Robotica: (2020) volume 38, pp. 699–718. © Cambridge University Press 2019
doi:10.1017/S0263574719000997

Dynamic Analysis of a Robotic Fish Propelled by Flexible Folding Pectoral Fins

Van Anh Pham†‡, Tan Tien Nguyen†, Byung Ryong Lee¶ and Tuong Quan Vo†*

†Ho Chi Minh City University of Technology, VNU-HCM, Ho Chi Minh City, Vietnam
E-mails: phamvananhhl@gmail.com, nttien@hcmut.edu.vn
‡ Pham Van Dong University, Quang Ngai, Vietnam
¶ School of Mechanical Engineering, University of Ulsan, Ulsan, Korea
E-mail: brlee@ulsan.ac.kr

(Accepted May 25, 2019. First published online: July 4, 2019)

SUMMARY

Biological fish can create high forward swimming speed due to change of thrust/drag area of pectoral fins between power stroke and recovery stroke in rowing mode. In this paper, we proposed a novel type of folding pectoral fins for the fish robot, which provides a simple approach in generating effective thrust only through one degree of freedom of fin actuator. Its structure consists of two elemental fin panels for each pectoral fin that connects to a hinge base through the flexible joints. The Morison force model is adopted to discover the relationship of the dynamic interaction between fin panels and surrounding fluid. An experimental platform for the robot motion using the pectoral fin with different flexible joints was built to validate the proposed design. The results express that the performance of swimming velocity and turning radius of the robot are enhanced effectively. The forward swimming velocity can reach 0.231 m/s (0.58 BL/s) at the frequency near 0.75 Hz. By comparison, we found an accord between the proposed dynamic model and the experimental behavior of the robot. The attained results can be used to design controllers and optimize performances of the robot propelled by the folding pectoral fins.

KEYWORDS: Folding pectoral fins; Flexible joint; Morison force; Propulsive efficiency; Strouhal number.

1. Introduction

Fish with million years of adaptation and evolution have been the master of underwater locomotion. Their prominent talents with speed, efficiency, and maneuverability have attracted attention of researchers in recent years.[1–6] Study results of physiology and morphology on fish fins structure and characteristic have oriented for designing and improving the propulsive system of the fish-inspired underwater vehicles.[7] For instance, George V Lauder et al. discovered three-dimensional (3D) kinematic, material properties, power and control, and fluid force effect on bluegill sunfish pectoral fin,[8] and Wang et al. extracted 3D motion of pectoral fin of a Koi Carp fish by digital image processing.[9] A remarkable understanding of the biological specification of fish fin movement allows us to solve the design challenges of the propulsive mechanism on robotic fish. For example, in refs. [10, 11], the design of an artificial pectoral fin with fin rays actuated by shape memory alloy wires was conducted in imitation of much complex motion of a Carp's fin. In ref. [12], a multi-degree of freedom (DOF) counterpart of pectoral fin of the bluegill sunfish was also developed to predict the propulsive force through the sensor system distributed within flexible fin ray. Researches on smart material enabled

---

* Corresponding author. E-mail: vtquan@hcmut.edu.vn

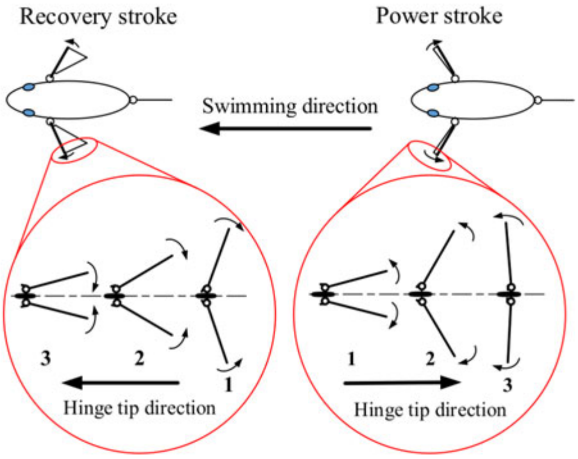

Fig. 1. Illustration of the movement of fin panels in strokes.

robotic pectoral fins to mimic many complex motions like the real fish pectoral fins. Nevertheless, this requires a large number of DOFs and increases complication of controllers.

On the other hand, the propulsive mechanism and the factors impacting on motion efficiency of the pectoral fin such as the shape of fins, the flexibility of fins, or joints were explored with empirical investigations for both real fish and robotic fish,[5,12,13] while the numerical simulation such as computational fluid dynamics (CFD) was paid attention by reliability and accuracy despite time-consuming computation.[14,15] More suitable for designing controllers, the analysis modeling for the pectoral fin has attracted attention in some recent researches[16–18] in which the blade element theory was used to establish hydrodynamic interactions. Different from the above approaches, analysis modeling using Morison's model has not mentioned to the robotic fish with the rowing pectoral fin.

In recent years, although some researches into pectoral fins have obtained a relatively comprehensive understanding of hydrodynamic interaction and the thrust-generating mechanisms, the pectoral fin with a folding structure which has the capability of reducing appreciable drag force in recovery stroke has not been noted yet. In ref. [19], the study on a robotic fin type with the variable area was reported. Its area is indeed adjusted by rotating a cover to shield holes on a base fin, while our research proposed a folding type of fin panels in a design of the robotic pectoral fin in rowing mode. The objective of this work is to improve the propulsive speed of robotic fish without causing pitch or roll motion to the robotic head part during swimming. Different from the mechanical designs presented in refs. [17, 18], our fin type composes two fin panels connected to a hinge peduncle through the flexible joints. It is noted that the thrust/drag area ratio in fin movement direction between recovery stroke and power stroke is scrutinized to minimize drag force, which is compared with a multi-DOFs fin structure in refs. [12,19]. Figure 1 illustrates a two-stroke cycle of the robotic swimming movement with the proposed pectoral fins. The component detail of each pectoral fin is introduced in Section 2.

In actuality, the motion of robotic fish with pectoral fins is diverse activities and complicated. The analysis modeling method is further appropriate to establish a dynamic model with proper accuracy[20] and acceptable computation time. In the present work, we used the Lagrange method, the Morison force, and the rigid body dynamics to describe the hydrodynamic relation among pectoral fins, body, and surrounding fluid.

The remaining of this paper is arranged into five sections as follows: Section 2 introduces the mechanical design for the folding pectoral fin and the robot prototype. The detail of the modeling proposals is presented in Section 3, including the dynamics of the pectoral fin and the body motion. The description of the experimental works and the parameter identifications are reported in Section 4. Section 5 presents the evaluation of attained result and discussions. Finally, the conclusions and direction of future work are provided in Section 6.

2. Mechanical Design

An intuitive demonstration, including the outside design of the robotic fish, the arrangement of the inside components, and the layout of electrical elements, is presented in Fig. 2. The robot is composed

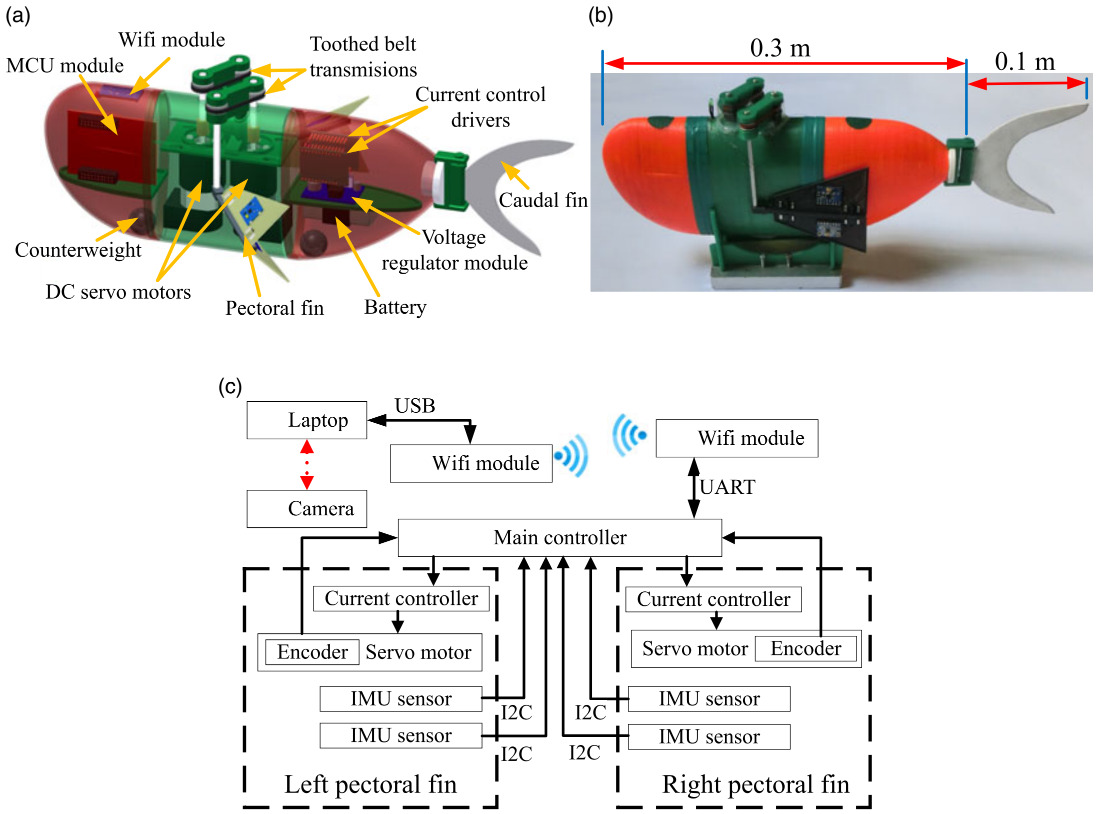

Fig. 2. Illustration of the designed robot: (a) the structural model, (b) the fabricated prototype, and (c) the layout of the electrical components (a dotted line (....) denotes an offline connection).

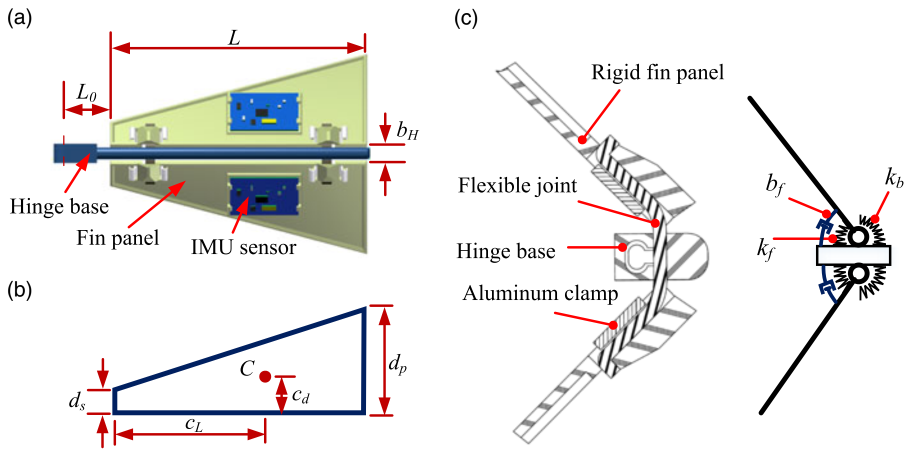

Fig. 3. Design of the folding pectoral fin: (a) the model of the pectoral fin attached inertial measurement unit (IMU), (b) the geometric sizes of the fin panel, and (c) the flexible joint and its equivalent diagram.

of a pair of folding pectoral fins, a passive rigid caudal fin, and a body part containing the electronic element and motors. The total length and mass of the robot are 0.4 m and 1.059 kg, respectively.

Each the pectoral fin is driven by a DC servomotor connected to hinge base through the toothed belt transmission. Figure 3 shows the detail of the pectoral fin design. The pectoral fin shape differs among fish as a consequence of swimming modes. In the drag-based swimming mechanism, R. W. Blake[21] claimed that the thrust generation on fish is more likely the triangle fins than square, rectangular, or truncated triangle ones. Triangle fin also causes less interference drag compared to square or rectangular one. Trapezoidal fin with a small baseline and a long leading edge was investigated

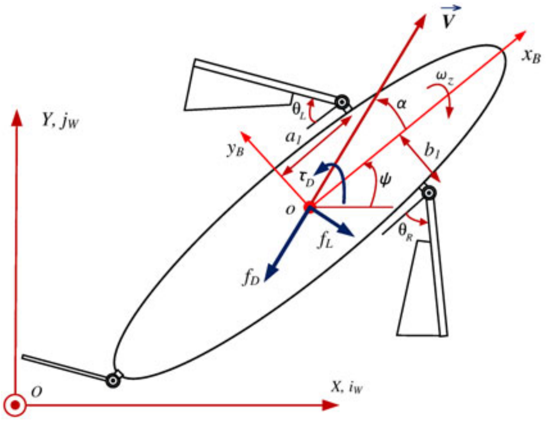

Fig. 4. Top view of a diagram of the fish robot in the two-dimensional plane.

since it is similar to many of natural counterparts.[22] Because of the above reasons, we choose a simple trapezoidal shape for each fin panel instead of reproducing the geometry of specific fish fin. The robot's pectoral fin on power stroke is almost like a triangle (such as Angelfish pectoral fin). On the other hand, the trapezoidal fin panel calculation is less complex. The distance from the shaft hole center of the hinge base to the shortest edge of the fin panel is $L_0 = 0.015$ m. The sizes of the fin panel are $d_s = 0.010$ m, $d_p = 0.040$ m, and $L = 0.080$ m; the width of the hinge base $b_H = 0.010$ m; and c_d, c_L are the coordinates of the geometrical center C of the fin panel. Masses of the hinge base and the fin panel are $m_H = m_F = 0.003$ kg. To easily acquire the angular displacement of each fin panel, a tilt sensor is attached to the geometrical center of each fin panel. We used a 3D printer with the polylactic acid (PLA) material to fabricate the fin panels and hinge base while the flexible joints are made of rubber. Figure 3(c) demonstrates a sectional structure and the equivalent model of the pectoral fin. Here, the equivalent stiffness of the flexible joint in "front region" and "back region" are abbreviated as k_f and k_b, respectively, with $k_b >> k_f$.

3. Dynamic Model

In this section, the dynamic model of the fish robot is established. The schematic diagram of the analytical model of robot motion in two-dimensional (2D) plane is illustrated in Fig. 4. Here $OXYZ$ indicates the inertial coordinate system and $ox_By_Bz_B$ identifies the body-fixed coordinate system located at the center of buoyancy of the fish robot. $[i_W, j_W, k_W]^T$ is the denotation of the unit vectors in inertial frames. We neglect the effectiveness of the 3D motion and pay attention to planar motion such as surge (v_x), sway (v_y), and yaw (ω_z). In the inertial frames, V denotes the velocity of the body part consisting of the surge velocity and the sway velocity, satisfying the following expression: $V = \sqrt{v_x^2 + v_y^2}$. α indicates the attack angle and satisfying $tg(\alpha) = \frac{v_y}{v_x}$; ψ is the directive angle of the robotic fish; and θ_L, θ_R are the angular position of the left and right fin. Note that the positive angle value is the counterclockwise direction. f_D, f_L, and τ_D are, respectively, the drag force, the lift force, and the drag moment of fluid flow exerted on the center of the body. The Morison force model is adopted to represent the inertial and drag effects of surrounding fluid impacting on the fin panel surfaces. The analytical schema of the right and the left pectoral fins is shown in Fig. 5.

The expressions describing the fluid force effects on the fin panel kth of pectoral fin K and the hinge base K over one length unit are expressed as follows:

$$dF_{Kk}(\ell, t) = -C_a\frac{\pi}{4}\rho_H d^2 a_{Kk}(\ell, t)d\ell - \frac{1}{2}C_d d\rho_H v_{Kk}(\ell, t)|v_{Kk}(\ell, t)|d\ell, \tag{1}$$

$$dF_{HK}(\ell_0, t) = -C_a\frac{\pi}{4}\rho_H b_H^2 a_{HK}(\ell_0, t)d\ell_0 - \frac{1}{2}C_d b_H\rho_H v_{HK}(\ell_0, t)|v_{HK}(\ell_0, t)|d\ell_0, \tag{2}$$

where $k = 1, 2$; K is subscript corresponding to left pectoral (L) or right pectoral fin (R). Note that the direction of these forces is reverse to the relative velocity of moving object. C_a and C_d are inertia and drag coefficients identified by fitting measurement data; ρ_H is the density of water; d is the width of a

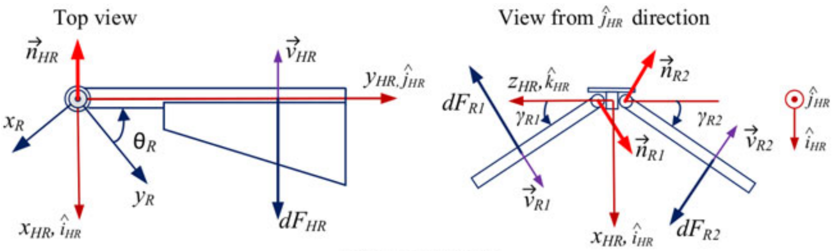

Right pectoral fin

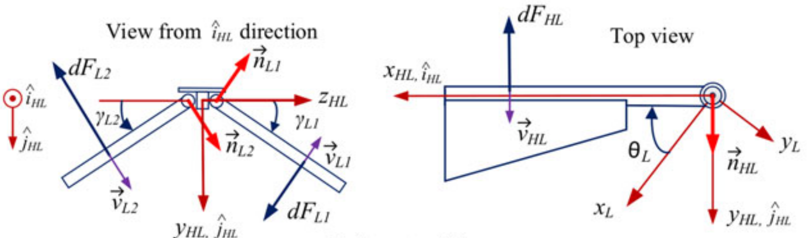

Left pectoral fin

Fig. 5. Analytical diagram of the right and left pectoral fins.

segment $d\ell$; b_H is the width of hinge link; v_{Kk} and a_{Kk} are, respectively, the velocity and acceleration of a segment center on fin panel kth of the pectoral fin K. These values are calculated by projecting the derivative of the segment center position with respect to time once and twice onto the segment's normal vector.[23] In detail, their expressions are $v_{Kk} = {}^{W}\dot{\vec{p}}_{Kk}^{T}\vec{n}_{Kk}$ and $a_{Kk} = {}^{W}\ddot{\vec{p}}_{Kk}^{T}\vec{n}_{Kk}$. Similarly, we also obtain the velocity and acceleration of points on the hinge base as follows: $v_{HK} = {}^{W}\dot{\vec{p}}_{HK}^{T}\vec{n}_{HK}$ and $a_{HK} = {}^{W}\ddot{\vec{p}}_{HK}^{T}\vec{n}_{HK}$. The normal vectors and the position vectors of points on fin panel and hinge base are reported in the Appendix.

The external moment exerting rotational displacement of fin panel around joint of the hinge is expressed by

$$M_{Kk} = \int_{0}^{L} \frac{d(\ell)}{2} dF_{Kk}(\ell, t). \tag{3}$$

The moments caused by Morison force on the actuator shafts of the hinge bases are computed as follows:

$$\begin{aligned} M_K^{shaft} = \int_{0}^{L_0+L} \ell_0 dF_{HK}(\ell_0, t) - \int_{0}^{L} (L_0 + \ell)\cos(\gamma_{K1}) dF_{K1}(\ell, t) \\ + \int_{0}^{L} (L_0 + \ell)\cos(\gamma_{K2}) dF_{K2}(\ell, t). \end{aligned} \tag{4}$$

To consider the motion of fin panels and hinge base, we use Lagrange approach. The kinetic energy of the hinge base of the pectoral fin K is given as follows:

$$T_{HK} = \frac{1}{2} m_H v_{CHK}^T v_{CHK} + \frac{1}{2} \omega_{HK}^T \Xi_{HK} \omega_{HK}. \tag{5}$$

where m_H, v_{CHK}, and ω_{HK} are the mass of the hinge base, the linear velocity, and angular velocity of the hinge base about mass center, respectively; $\Xi_{HK} = {}^{W}R_{HK} I_{HK} {}^{W}R_{HK}^{T}$, and I_{HK} is the inertial tensor about a center of mass with regard to the coordinate axes of the hinge base K. The kinetic energy of each fin panel element kth of the pectoral fin K is written as follows:

$$T_{Kk} = \frac{1}{2} m_F v_{CKk}^T v_{CKk} + \frac{1}{2} \omega_{Kk}^T \Xi_{Kk} \omega_{Kk}. \tag{6}$$

Similarly m_F, v_{CKk}, and ω_{Kk} are, respectively, the mass of a fin panel, the linear velocity, angular velocity of the fin panel about its mass center; $\Xi_{Kk} = {}^{W}R_{Kk} I_{Kk} {}^{W}R_{Kk}^{T}$, and I_{Kk} denotes the inertial tensor about a mass center expressed in the frame attached to the fin panel Kk. Because the effects of buoyant force and gravity force on fin panels cause motion, hence we additionally consider their energy. We achieve the total potential energy of fin panels as follows:

$$P_K = \frac{1}{2}\sum_{1}^{2} k_\gamma \gamma_{Kk}^2 + m_{BG} g c_d (\cos(\gamma_{K1}) - \cos(\gamma_{K2})). \tag{7}$$

where γ_{Kk} is the angular position of fin panel (see Fig. 5); k_γ denotes the equivalent stiffness of the joint whose magnitude depends on the position of the corresponding fin panel (see Fig. 3(c)); g denotes the gravitational acceleration; $m_{BG} = (\rho_F - \rho_H)V_F$; and ρ_F and V_F are the mass density of fin material and the volume of fin panel, respectively.

Lagrange function, total virtual work, and Lagrange equation describing the motion of the pectoral fins are presented in Eqs. (8), (9), and (10), respectively:

$$L = T_{HL} + T_{HR} + \sum_{k=1}^{2}\big(T_{Lk} + T_{Rk} - (P_{Lk} + P_{Rk})\big), \tag{8}$$

$$\delta W = \delta W_L + \delta W_R + \sum_{k=1}^{2}\big(\delta W_{Lk} + \delta W_{Rk}\big), \tag{9}$$

$$\frac{d}{dt}\left(\frac{\partial L}{\partial \dot{q}_f}\right) - \frac{\partial L}{\partial q_f} = \frac{\partial \delta W}{\partial \delta q_f}, \tag{10}$$

where $\delta W_K = (\tau_K + M_K^{shaft} - b_M\dot{\theta}_K)\delta\theta_K$; $\delta W_{Kk} = (M_{Kk} - b_f\dot{\gamma}_{Kk})\delta\gamma_{Kk}$; b_M and b_f are the damping coefficients of actuator system and flexible joints, respectively; τ_L and τ_R are the DC motors' moments producing motion for the pectoral fins. $q_f = [\theta_L, \gamma_{L1}, \gamma_{L2}, \theta_R, \gamma_{R1}, \gamma_{R2}]^T$ is the generalized coordinates.

Under the assumptions that inertial coupling between the motions of sway, surge, and yaw is neglected, the dynamic equation in a plane of a rigid body is governed by Kirchhoff's equation and written as follows:[24]

$$\begin{cases} (m_b + m_x)\dot{v}_x = (m_b + m_y)v_y\omega_z + F_x, \\ (m_b + m_y)\dot{v}_y = -(m_b + m_x)v_x\omega_z + F_y, \\ (J_b + J_z)\dot{\omega}_z = (m_x - m_y)v_x v_y + M_z. \end{cases} \tag{11}$$

where m_b and J_b denote the mass of body and the body inertia about z-axis; m_x, m_y, and J_z represent the effects of the added mass and the added inertia of surrounding fluid on the body; F_x, F_y, and M_z are the external forces and moment acting on the center of the body. These include elements generated by the pectoral fins, and the interaction between the body and fluid. Their expressions are calculated as follows:

$$\begin{cases} F_x = T_R s(\theta_R) + T_L s(\theta_L) + f_L s(\alpha) - f_D c(\alpha), \\ F_y = -T_R c(\theta_R) - T_L c(\theta_L) - f_L c(\alpha) - f_D s(\alpha), \\ M_z = T_R(-a_1 c(\theta_R) + b_1 s(\theta_R)) - T_L(a_1 c(\theta_L) + b_1 s(\theta_L)) + \tau_D - \tau_L - \tau_R. \end{cases} \tag{12}$$

The thrust forces generated by the pectoral fin on the body are represented by T_L and T_R and are calculated as follows:

$$T_K = -\int_0^L \cos(\gamma_{K1})dF_{K1}(\ell, t) + \int_0^L \cos(\gamma_{K2})dF_{K2}(\ell, t) + \int_0^{L_0+L} dF_{HK}(\ell_0, t). \tag{13}$$

Additionally, the external forces and moment of the fluid acting on the mass center of the robot body are determined as follows:[25,26]

$$\begin{cases} f_D = 0.5\rho_H V^2 S C_D, \\ f_L = 0.5\rho_H V^2 S C_L \alpha, \\ \tau_D = -C_M \omega_z^2 sign(\omega_z), \end{cases} \tag{14}$$

where S are the wetted area of the body. C_D, C_L, and C_M denote the drag force coefficient, lift coefficient, and drag moment coefficient, respectively, $sign(.)$ represents the signum function.

Finally, the kinematic relationship of robot motion between the inertial frames and the body fixed frames is presented as follows:[27]

$$\begin{cases} \dot{X} = v_x \cos\psi - v_y \sin\psi, \\ \dot{Y} = v_x \sin\psi + v_y \cos\psi, \\ \dot{\psi} = \omega_z. \end{cases} \tag{15}$$

Combining Eqs. (11) and (15), the motion dynamics of the robot body is governed by a second-order differential equation with generalized coordinates: $q_b = [\psi, X, Y]^T$.

4. Experimental Description and Parameter Identification

This part describes the detail of the empirical works conducted to determine the concerned parameters and validate the swimming performance of the robot.

4.1. Experimental setup for testing the robotic fish swimming performance

First, the swimming motion of the robotic fish was conducted in a tank 2 × 1 × 0.5 m (L × W × H). The high-speed camera Casio ZR1000 combining a resolution 1920 × 1080 pixels and the frame rate 30 (fps) is hanged on the overhead of the tank to record the swimming velocity and turning radius of the fish robot. To generate the motion of the pectoral fins, the servomotors MOOR AS780D-131E were operated through current controllers Maxon Escon Module 24/2. The control unit of the robot is the evaluation board Tiva-TM4C123G. With this controller, the positional data of the hinge bases and the fin panel, and control command were transmitted and received between the robot and a computer through the wireless modules Zigbee-UART CC2530. Additionally, a led lamp attached to the robot back is used to notify the starting time in the transient state while tracking the robot motion using the camera. The position of hinge base is feedback through the motor encoder with resolution 2024 pulse per round, while the displacement angle of the fin panel is measured by IMU sensor GY-86 attached on each of fin panel (see Fig. 2). The reason for this is to reduce the measurement complexity, which is difficult to obtain with using cameras, especially when the robot moves. For example, in ref. [17], the authors had to anchor their robot to be able to measure the feathering angle of fins by using cameras. A demonstration diagram of the experimental system is summarized in Fig. 6.

4.2. Determination of the pectoral fin parameters

In this subsection, the stiffness and damping coefficients of joints are calculated through the experimental measurement of the angular deformation and the decay rate of the under-damped vibration for the fin panel in the air. Figure 7(a) and (b) shows the detail of the measurement of joint coefficients. The camera was adjusted to record the motion of fin panel at speed 240 frame per second and a resolution 512 × 384 pixels. In order to estimate the equivalent damper of joints, we assume that these damping coefficients are modeled as constant and measured through the experiment of the free decay vibration motion of a fin panel in the air. The ratio of relative damping is determined by measuring the logarithmic decrement: $\zeta = \frac{b_f}{b_{cr}} = \frac{b_f}{2\sqrt{k_f J_p}}$ is determined by measuring the logarithmic decrement δ, where J_p indicates the inertial moment of fin panel about the pivot of joint, $\delta = \ln(\frac{x_i}{x_{i+1}}) = \frac{2\pi\zeta}{\sqrt{1-\zeta^2}} \approx 2\pi\zeta$, where x_i, x_{i+1} are the displacement magnitude of the consecutive peaks ith and $(i+1)$th. Therefore, the damping coefficient is calculated as follows: $b_f \approx \frac{1}{\pi}\sqrt{k_f J_p}\ln(\frac{x_i}{x_{i+1}})$.

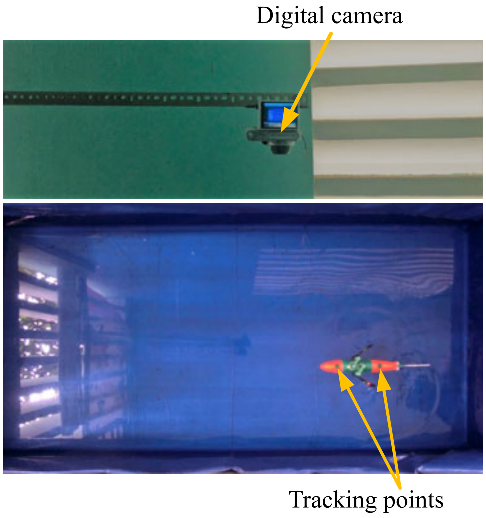

Fig. 6. Tracking experiment of the swimming motion of the robot.

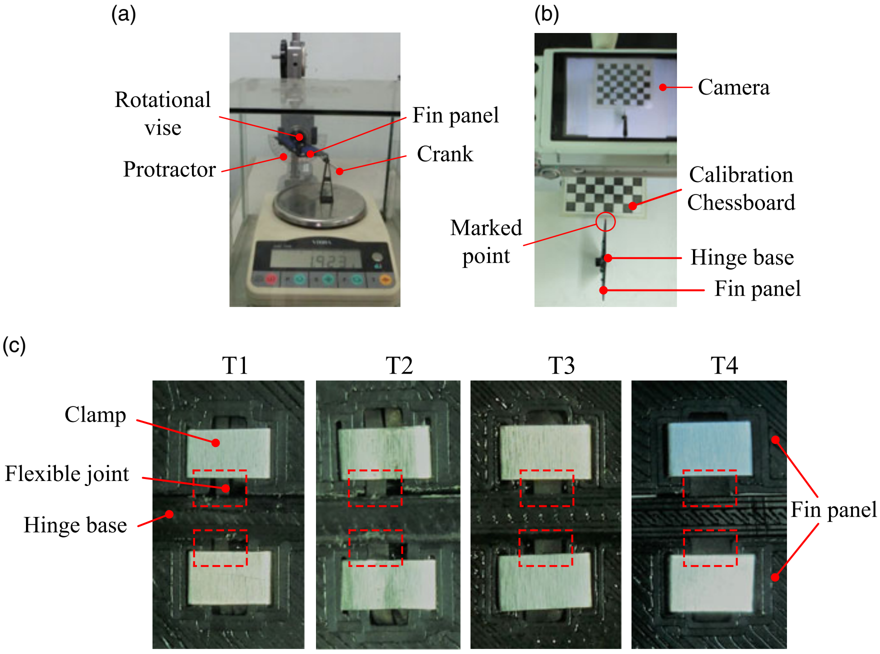

Fig. 7. Measurement experiment setup: (a) the joint stiffness, (b) the joint damping, and (c) four flexible joint types for experiments.

We used four fin types, named T1, T2, T3, and T4, differing about the flexible joints, with 1 mm of thickness and 1.1, 1.6, 2.3, and 3.7 mm of width, respectively (see Fig. 7(c)). Table I provides the average values of the spring stiffness coefficients: k_f, k_b and damping coefficients b_f estimated by experiments. These values will be employed to evaluate the proposed dynamic model.

4.3. *Determination of the stroke ratio and amplitude ratio*

To generate cyclical motion of the pectoral fins, the servomotors were programmed to produce moment curve under the sine waveform. However, because the fluid load acted on the moving direction of the pectoral fin has a large discrepancy between the power stroke and the recovery stroke, a modified waveform was used as follows:

$$\tau(t) = \begin{cases} P_r \sin(\dfrac{\pi}{T_r}(t - NT_w)), & \textit{if} \quad NT_w \leqslant t < (NT_w + T_r), \\ P_p \sin(\frac{\pi}{T_p}(t - NT_w - T_r) + \pi), & \textit{else} \;\; t \geqslant (NT_w + T_r). \end{cases} \tag{16}$$

https://doi.org/10.1017/S0263574719000997

Table I. The stiffness and damping values of the joints.

Fin types	k_f**(N/rad)**	k_b**(N/rad)**	b_f**(Ns/rad)**
T1	0.20^{-3}	$4.62 \cdot 10^{-3}$	$3.48 \cdot 10^{-6}$
T2	0.30^{-3}	$7.98 \cdot 10^{-3}$	$4.25 \cdot 10^{-6}$
T3	0.32^{-3}	$12.08 \cdot 10^{-3}$	$4.03 \cdot 10^{-6}$
T4	0.65^{-3}	$17.27 \cdot 10^{-3}$	$3.80 \cdot 10^{-6}$

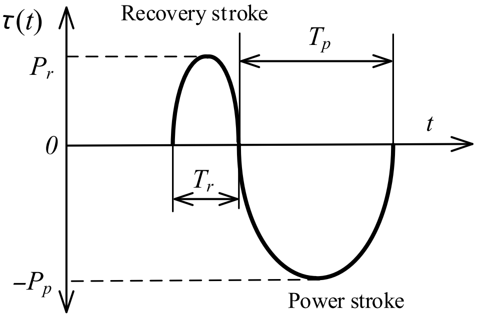

Fig. 8. Illustration of the torque curves corresponding to recovery stroke and power stroke.

where $N = floor(\frac{t}{T_w})$; $floor(.)$ is the round function to a nearest integers toward minus infinity. $T_w = T_r + T_p = \frac{1}{f}$; f denotes the input frequency; P_r, P_p are the peaks of the torque curve shown in Fig. 8. In this paper, the average amplitude of moment is given by $P_m = \frac{P_p+P_r}{2}$.

On the other hand, fluid disturbance generated by the combination of swimming motion of the robot and the pectoral fin can cause negative effects as the drift phenomenon of the motion direction of fins. For this reason, an improved form-based amplitude modulation mechanism[28] will be substituted to the torque curve and described as follows:

$$\begin{cases} \tau_R = \tau(t)\left(1 + k_\triangle \left(\theta_R - \theta_R^{ref}\right) sign\left(\tau(t)\right)\right), \\ \tau_L = -\tau(t)\left(1 + k_\triangle \left(\theta_L - \theta_L^{ref}\right) sign\left(-\tau(t)\right)\right), \end{cases} \tag{17}$$

where θ_R^{ref} and θ_L^{ref} denote the reference angles corresponding to the right and left pectoral fins. Each fin panel of the pectoral fin operates as a paddle, so, for a facility, the reference direction of the pectoral fins is chosen as follows: $\theta_R^{ref} = 90°$, $\theta_L^{ref} = -90°$; $k_\triangle$ is the proportional coefficient and chosen by $k_\triangle = 0.48$ for all simulation and swimming experiments. It means that if average direction error equals 10°, the amplitude of moment will adjust by 8.4%.

The free-swimming experiments are firstly conducted for the T2 fin type to consider the effect of ratios ε_T, ε_P defined, respectively: $\varepsilon_T = \frac{T_r}{T_p}$, $\varepsilon_P = \frac{P_p}{T_r}$ on the swimming velocity. Figure 9 provides a comparison within a range of ratios $\varepsilon_T = \{0.25; 0.5; 1; 2; 3; 4\}$, $\varepsilon_P = \{1; 2; 3; 4\}$ and the forward velocity for fin type T2. The average forward velocity values are calculated by $\bar{V} = \frac{1}{T_w}\int_{t_0}^{t_0+T_w} V(t)dt$, with t_0 is the beginning of steady state. In these experiments, the average amplitude is $P_m = 0.0156$ N m, and it is also used for all the independent experimental works later. From Fig. 9, it can be observed that the robot attains the highest forward velocity with $\varepsilon_T = 1$ and $\varepsilon_P = 3$. These ratios are used for all different joint types with each swimming mode then. We carried out all experiments with 10 repeated times to restrict the effect of random disturbance.

4.4. Determination of the different parameters

Next, the parameters for the simulation are directly measured or calculated from experimental prototype and then reported in Table II. For simplification, the added masses and added inertia are calculated by approximating the shape of the robotic body as a prolate spheroid.[29]

Table II. Value of the parameters of the robot.

$m_b = 1.0410$ kg	$\rho_H = 1000$ kg/m^3	$I^l_{CF} = 7.36.10^{-7}$kg m^2
$m_x = 0.0749$ kg	$S = 0.0722$ m^2	$I^t_{CF} = 12.69.10^{-6}$ kg m^2
$m_y = 0.9145$ kg	$a = 0.160$ m	$I^w_{CF} = 11.97.10^{-6}$ kg m^2
$J_b = 0.0055$ kg m^2	$a_1 = 0.034$ m	$I^e_{CF} = -2.54.10^{-6}$ kg m^2
$J_z = 0.0036$ kg m^2	$b = 0.026$ m	$I^w_{CH} = I^t_{CH} = 7.5.10^{-6}$ kg m^2
$\rho_F = 1209$ kg/m^3	$b_1 = 0.032$ m	$I^l_{CH} = 1.6.10^{-8}$ kg m^2

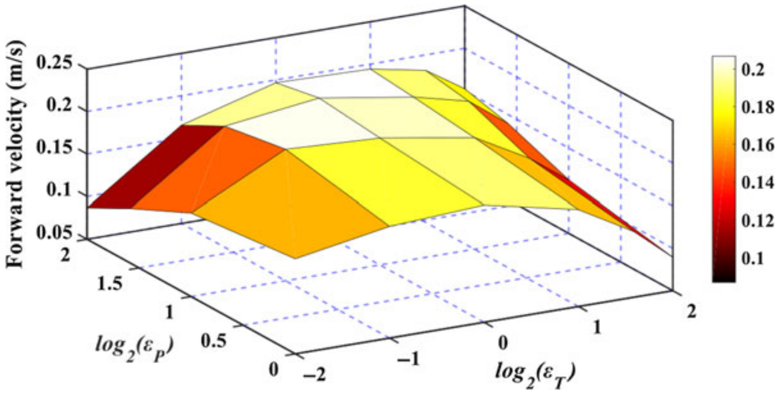

Fig. 9. Dependence of the forward swimming velocity of the fin type T2 on ε_T, ε_P at the frequency of 0.5 Hz.

Finally, to gain a deeper insight into the dynamic relationship between the motion of the rigid body part and the fins, the coefficients of drag force C_D, lift force C_L, and drag moment C_M need to be determined. Some previous researches used simulation approach or through experiment. For example, while the parameters C_D, C_L, and C_M were obtained through CFD simulation,[24] they could be found through matching data between simulation and experiment under the mode of turning and forward swimming.[17,18,30] For our work, an experimental identification is more priority due to accuracy under practical condition. The coefficient C_D is first determined by the underwater movement measurement of the robot body through pulleys and a rope connected to a free falling object,[31] and the resulting value is $C_D = 0.0175$. Then the coefficients C_L, C_M, C_a, and C_d are simultaneously identified by minimizing data in the turning swimming mode. These data include relative errors between experiment and simulation corresponding to the average turning radius, the average turning velocity, and the position of hinge base in the frequency range from 0.5 Hz to 2.25 Hz with step 0.25. The resulting coefficients $C_L = 9.8875$ and $C_M = 0.0123$ are the best values obtained from the optimization issue. Three coefficients are then used for simulations evaluating the proposed model through the free-swimming performance of the robot in both transient state and steady state.

5. Results and Discussion

This part describes and discusses the results derived from simulation and experimental works. These results include the straight swimming and turning performances in both the transient state and the steady state of the robot. Additionally, the evaluation of energy expenditure, cost of transport (COT), propulsive efficiency, and the Strouhal number is also considered to determine the efficient swimming range.

5.1. Effect of the flexibility of joints on the swimming performance

The stiffness of the flexible joints directly affects the performance of swimming speed and turning radius. The experiments on four different flexible joint types were conducted for the same amplitude value of the test moment and frequency varied from 0.5 up to 2.25 Hz. Figures 10 and 11 highlight the forward swimming and turning swimming speed of the robot, notified in both unit m/s and unit BL/s (body length per second). The obtained swimming speed is the highest in the frequency range from 0.75 to 1 Hz. Comparing the flexibility of joints, the type T4 with the highest joint stiffness obtains the lowest swimming speed range. The highest speed of the fin T2 is 0.231 m/s (0.58 BL/s) and 0.147

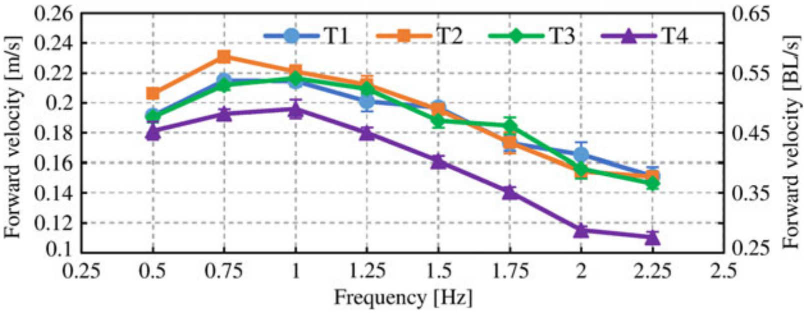

Fig. 10. Experimental comparison of the forward swimming velocity of the fin prototypes with the different frequencies.

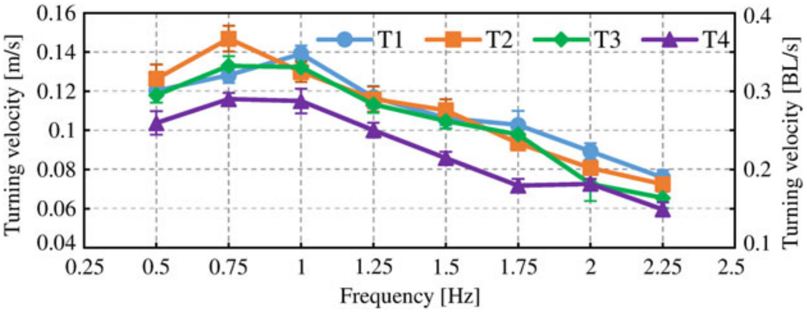

Fig. 11. Experimental comparison of the turning velocity of the fin prototypes with the different frequencies.

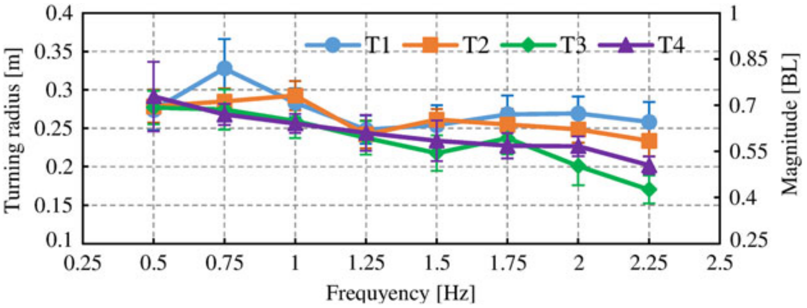

Fig. 12. Experimental comparison of turning radius of the fin prototypes with the different frequencies.

m/s (0.37 BL/s) for the straight swimming mode and the turning mode, respectively. In particular, the frequency in which the types of fins T3, T4 attain the highest forward velocity is higher than the one of fin types T1, T2 in the straight swimming mode. There is an incoherent difference between the speed performances corresponding to the joints T1, T2, T3 in the higher frequency range of 1 Hz. On the other hand, the experimental results showed that the velocity v_x decreases as the frequency increases from 1 Hz. The peak of velocity performance lies in the low-frequency range. The reason is ascribed to the discrepancy increase of the drag/thrust areas corresponding to recovery/power strokes of each pectoral fin in the low-frequency range. Figure 12 provides the relationship of turning radius versus frequency corresponding the pectoral fin types. Generally, the radius values reduce as the frequency increases. The difference of turning radius performance is really ambiguous for the fin types. In the tested frequency range, the turning radius of the fin T3, T4 is generally lower than the others. This implies that the robot with the less flexible joints can attain the smaller turning radius.

5.2. *Performance for transient state*

This subsection describes the evaluation of the proposed dynamic model in a transient state. The fin type T2 is taken into account because the robot could achieve the best swimming performance while using this type. We conduct some simulations at the rowing frequency 0.75 Hz. Note that this is also

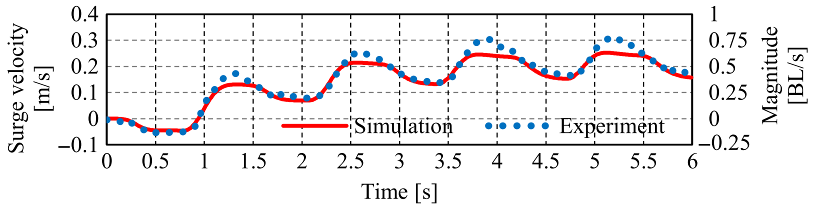

Fig. 13. Performance of the surge swimming velocity.

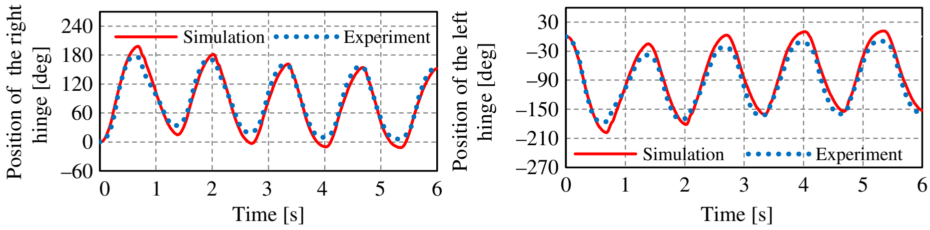

Fig. 14. Position performance of the hinge base: (a) right hinge and (b) left hinge.

the frequency where the experimental robot reaches the highest experimental forward velocity. To assess the accuracy of the proposed mathematical model, we observe intuitively and calculate the normalized root mean squared error (nRMSE) to compare the simulation and experimental results. The expression of nRMSE for the forward swimming velocity is defined as

$$\triangle v_x = \sqrt{\frac{1}{N}\sum_{i=1}^{N}\left(\frac{v_x(i) - v_x^{exp}(i)}{\bar{v}_x^{exp}}\right)}. \tag{18}$$

where $v_x^{exp}(i)$ and $\bar{v}_x^{exp}$, respectively, are the ith experimental velocity and the average experimental velocity calculated in steady state. Similarly, we can derive the values of nRMSE for the positions of the right hinge base, left hinge base, the above right fin panel, the below right fin panel, the above left fin panel, and the below left fin panel, named $\triangle\theta_R$, $\triangle\theta_L$, $\triangle\gamma_{R1}$, $\triangle\gamma_{R2}$, $\triangle\gamma_{L1}$, $\triangle\gamma_{L2}$, respectively. The parameters C_a, C_d are tuned by the trial-error method through the observation and quantified by using Eq. (18), and the values are obtained as follows: $C_a = 0.15$, $C_d = 1.62$. Figures 13, 14, and 15 show the transient responses of the surge velocity, the hinge motion position, and the position of the fin panels, respectively. We indicate that the motion of pectoral fin hinge nearly sweeps the hold of the body side space. This helps the robot attain high velocity. The experimental data strongly support the simulation one, especially in the surge swimming velocity and the hinge position performances. A small amount of error existing on the responses of the fin panel position can be due to the complex interaction of fluid along the fin panels in the generation of waves.

The left turning performances of the robot, in the transient state, are shown in Figs. 16–18. There is a relatively good agreement between experiment and simulation indicated on the turning velocity and the position of the hinges, though little errors also exist in the position performance of the fin panels.

To quantify the error assessment between experimental and simulation results, we calculate nRMSE for the parameters including the surge swimming velocity, the position of hinges, and fin panels. Table III reports nRMSE values. In the straight swimming mode, the nRMSE values are small. These show that the experiment performances well agree with the simulation ones. In turning swimming mode, most of the nRMSE values are relatively small. However, the nRMSE value of the left hinge position is significantly larger than the others; this can be because the left pectoral fin is drifted by fluid disturbance while its position is not driven. Overall, the result data claimed that the proposed dynamic model well predicted the behavior of the real system in the transient state.

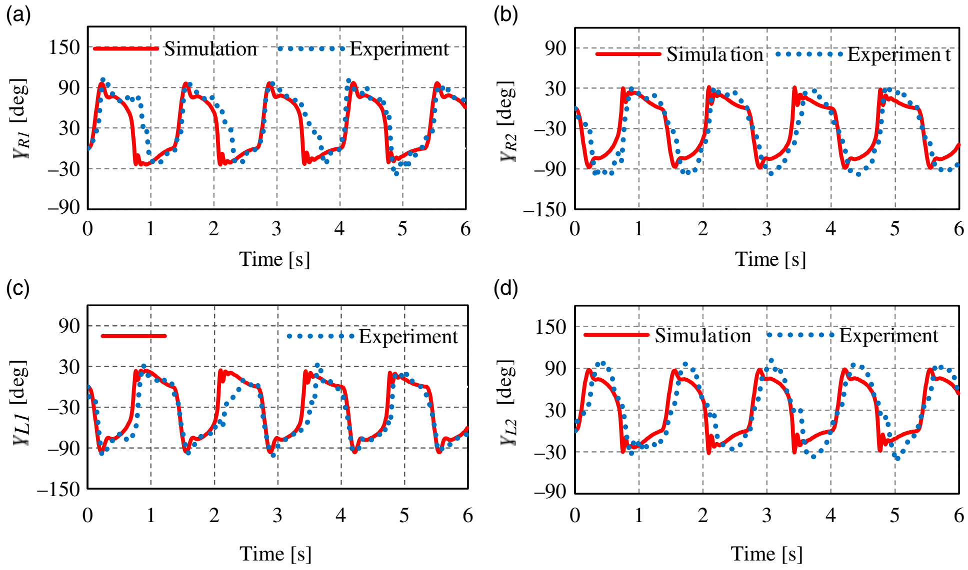

Fig. 15. Position performance of the fin panels: (a) below right fin panel, (b) above right fin panel, (c) below left fin panel, and (d) above left fin panel.

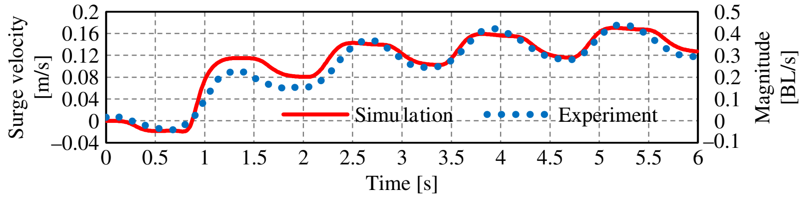

Fig. 16. Performance of the surge swimming velocity.

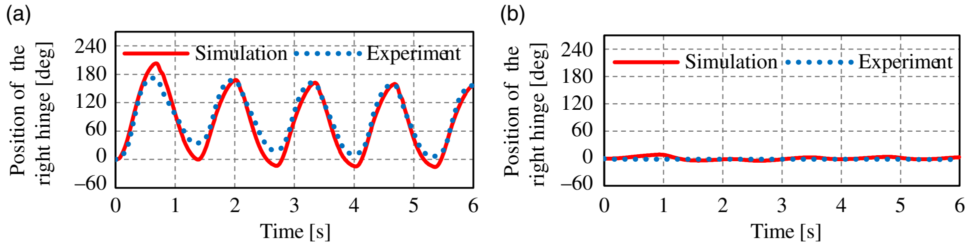

Fig. 17. Position performance of the hinge base: (a) right hinge and (b) left hinge.

5.3. *Performance for steady state*

For further validating the proposed model of the fish robot with type T2, the comparison between experimental and simulation performances in the steady state was implemented. Figures 19 and 20 show the average surge velocity of the straight swimming and turning swimming mode, respectively. In both modes, it is clear that the surge velocity increases and reaches the highest value at the frequency of 0.75 Hz, and then decreases with the rise of the rowing frequency. There are several discrepancies in the experiment and simulation result. However, the variation tendency of velocities in the simulation is still similar to the experiment result. The average relative errors of surge velocity in the forward swimming and turning mode are 8.9% and 15.8%, respectively. We additionally compare the turning swimming radius between experiment and simulation. Figure 21 illustrates the relationship between turning radius performance versus the frequency. It is easy to see that the variation of the average turning radius following the frequencies is relatively small. The simulation values of turning radius are close to the experimental ones. The average relative error is 9.5%. The reason for the complete non-coincidence of the experiment and simulation response can be due to

Table III. nRMSE of the robot parameters.

Mode	**Straight swimming**	**Turning**
$\triangle v_x$	0.0039	0.0044
$\triangle \theta_R$	0.0068	0.0097
$\triangle \theta_L$	0.0076	0.0939
$\triangle \gamma_{R1}$	0.0294	0.0314
$\triangle \gamma_{R2}$	0.0301	0.0342
$\triangle \gamma_{L1}$	0.0221	0.0419
$\triangle \gamma_{L2}$	0.0298	0.0330

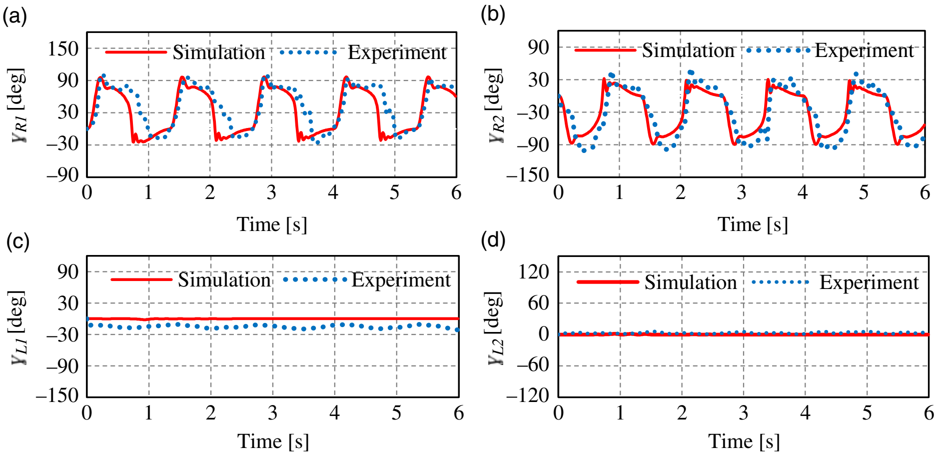

Fig. 18. Position performance of the fin panels: (a) above right fin panel, (b) below right fin panel, (c) above left fin panel, and (d) below left fin panel.

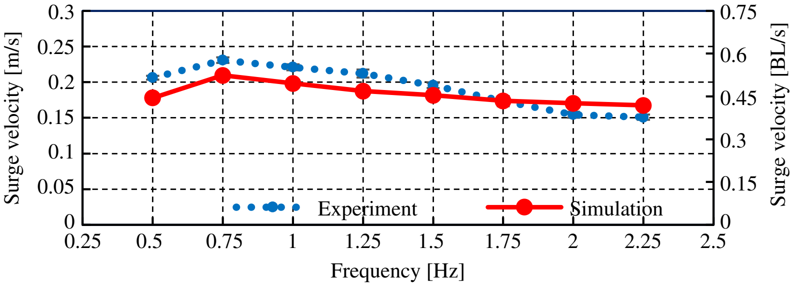

Fig. 19. Straight swimming velocity performance of simulation and experiment.

the influence of interaction with backward fluid disturbance from tank wall on the robot. Generally, the performance of the proposed model well predicted the feature of the real robot.

In summary, it can be seen that the simulation performances in both the transient state and steady state of free-swimming mode are in agreement with the experimental ones. We can conclude that the proposed dynamic model successfully predicts the motion behavior of the fish robot.

5.4. Power expenditure, cost of transport, propulsive efficiency, and Strouhal number

To assess the level of energy expenditure of the robot, we consider average input power $\bar{P}_i$ and the cost of transport:[32] COT $= \frac{\bar{P}_i}{m_R \bar{V}}$, where $\bar{P}_i$ and m_R are the average input power and the total dry mass of the robot, respectively. The expression of the input power is presented in the Appendix, $m_R = m_b + 4m_F + 2m_H$. Figure 22 records the performance of the average power expenditure and COT in relationship to the frequency of the pectoral fins. It shows that the input power is smaller than 102 mW and COT in range of 0.42–0.58 (J/kg/m) or 0.17–0.23 (J/kg/BL). The values of COT lies in a

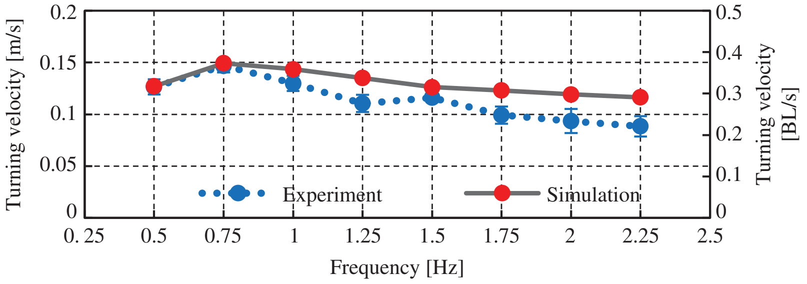

Fig. 20. Turning velocity performance of simulation and experiment.

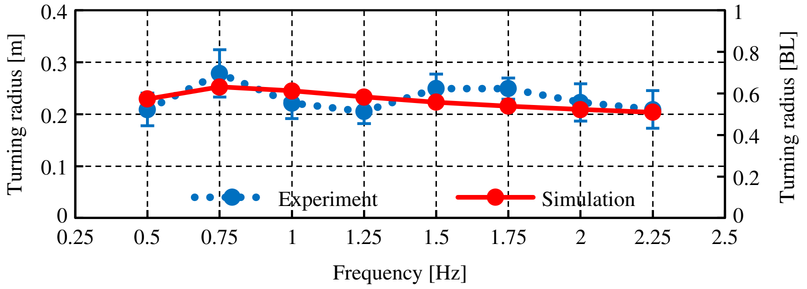

Fig. 21. Turning radius performance of simulation and experiment.

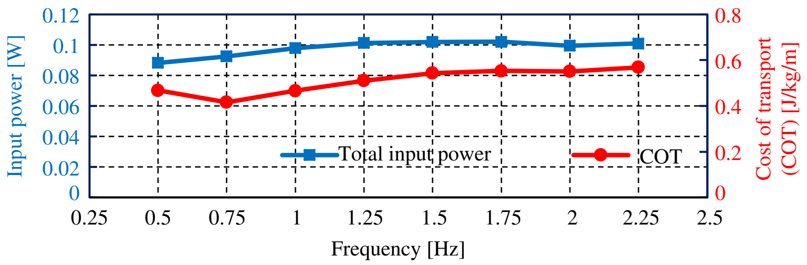

Fig. 22. Power expenditure and cost of transport in the straight swimming mode.

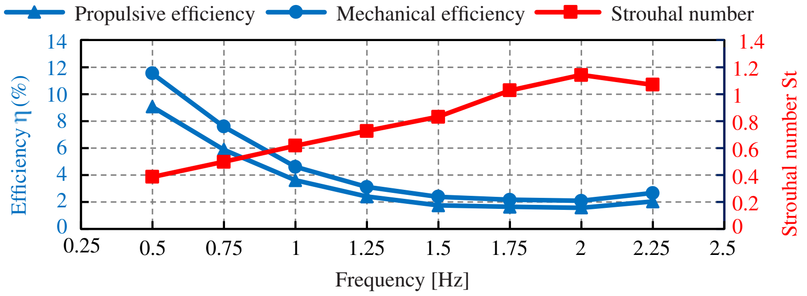

Fig. 23. Propulsive efficiency, mechanical efficiency, and Strouhal number in the straight swimming mode.

range from 0.10 to 0.27 (J/kg/BL) of a few median paired fin (MPF) fish at the same swimming speed range.[33] This claims that, in MPF swimming, the energy expenditure cost of the robot is equivalent to natural fish at the same speed range.

On the other hand, we also consider the propulsive efficiency and the mechanical propulsive efficient in the steady-state forward swimming, correspondingly defined as follows:[6, 34] $\eta = \frac{\bar{P}_o}{\bar{P}_i}$, $\eta_m = \frac{\bar{P}_o}{\bar{P}_{mi}}$, where $\bar{P}_o$ and $\bar{P}_{mi}$ are the average output power and the average mechanical power, respectively. The detail of these power expressions is explained in the Appendix. Figure 23 illustrates the propulsive

Table IV. The swimming performance comparison of several searches.

References	The highest average speed	Average turning radius
Ref. [16]	0.045 m/s (0.33 BL/s)	0.16–0.18 m (1.07–1.20 BL)
Ref. [17]	0.040 m/s (0.27 BL/s)	0.16–0.23 m (1.07–1.53 BL)
Ref. [18]	0.045 m/s (0.30 BL/s)	0.23–0.24 m (1.53–1.60 BL)
Ref. [37]	0.035 m/s (0.09 BL/s)	–
Present study	0.231 m/s **(0.58 BL/s)**	0.25–0.33 m **(0.63–0.83 BL)**

Note: The bold values in Table IV show the obtained robot speed is faster (value of straight speed is higher) and more maneuverable (turning radius is smaller) compared to corresponding parameters in previous searches.

efficiencies of the robot. This performance indicates that the robot swims more efficiently at lower frequencies. A slight difference between the total propulsive efficiency and the mechanical efficiency is due to a frictional loss on the motors and the transmission system. In the range of survey frequencies, the highest mechanical efficiency is only 11.53%. A report showed that the total propulsive efficiency for drag-based labriform locomotion is 16%[35], while the maximum propulsive efficiency of labriform swimming can reach 31% for rigid rays and 36% for flexible rays.[22] In ref. [36], mechanical efficiency of the pectoral fin in three-spine stickleback fish is from 10% to 30%. Compared to the above fish locomotion, the achieved efficiency in our research is relatively low.

To provide additional insight into the dynamic performance of the robot, the Strouhal number, a parameter quantifying frequency, amplitude, and swimming speed for the optimal range of swimming movement, is considered. Its expression is defined as follows:[37–39] $St = \frac{fA}{V}$, where A is defined as the excursion length (peak to peak) of the tip of fin panel and is approximated as follows: $A \approx \sqrt{4L^2 \sin^2\left(\frac{\theta_R}{2}\right) - 2Ld_s \sin(\theta_R) + d_s^2}$. Figure 23 illustrates the relationship between the Strouhal number and frequency. At the frequency 0.75 Hz, the Strouhal number is 0.5 that is near optimal swimming range from 0.2 to 0.4 in ref. [40]. An extensive range of optimal Strouhal number from 0.15 to 0.8 mentioned in ref. [41] was exploited by considering the kinematics of 53 different aquatic species. Thus, with proposed fin type, there is existent of a range of low frequencies where the robotic fish performance lies in the region of the high swimming velocity, acceptable efficiency, and nearly optimal range of the Strouhal number.

Additionally, our robot's swimming parameters are compared to a natural counterpart, Angelfish.[42] This fish uses pectoral fins in the rowing swimming mode and keeps the tail fin inactive. The swimming data show that Angelfish can obtain the propulsive efficiency of 0.18 and the steady forward speed of 0.5 BL/s. These parameters indicate that our robot moves at a similar swimming speed, but the propulsive efficiency is little lower than that in natural Angelfish. Finally, to further clarify the advantage of the proposed pectoral fin type, a collection of the swimming speed and the turning radius in some concerned researches is reported in Table IV. The attained performances of the average swimming speed and the average turning radius in this research are very competitive. The robotic fish in this research can reach the high movement velocity, and the optimal range quantified by Strouhal number is close to the efficient swimming region. The energetically used efficiency is near equivalent fish. However, the propulsive efficiency is not equal to natural fish. Thus, the improvement of the propulsive efficiency for the robot with the folding pectoral fins is a challenging issue in the future work.

6. Conclusion

This paper has proposed the dynamic model for the robotic fish propelled by the folding pectoral fins. The novel type of these pectoral fins produced high swimming velocity for the robot. We established the robot motion description equations in the combination of the Lagrange method, Morison force model, and the rigid body dynamics. Through a serial of the empirical works, the swimming performance of the fish robot with four different joint types were compared. The straight swimming speed and turning radius were significantly improved in comparison with previous researches. In particular, the matching between the simulation results and experiment ones shows that our proposed dynamics model can predict the real motion of the robot relatively well. Moreover, with a joint type which the robot obtains the fastest swimming speed, the rowing frequency for the highest of velocity is near 0.75 Hz, and the Strouhal number also lies near the optimal swimming range. The energy expenditure is similar to natural fish at the same swimming velocity range. The design of this fin type and the proposed dynamic model will facilitate the improvement to velocity, maneuverability, and designing controllers for fish robots using the pectoral fins. There are several directions where future work will be addressed as follows: first, we will consider the multi-object optimization issue for the swimming speed and propulsive efficiency where inputs are the geometrical parameters of the fin and the flexibility of joints. Second, the analysis of performance for the folding fin types with the flexible fin panels instead of the rigid ones will be exploited. Finally, we can also expand the investigation of the robot dynamic propelled by the folding pectoral fins for the robotic 3D motion case, in which, the deep steering direction is controlled through the robot center variation mechanism or directional angle of the pair of pectoral fins.

Acknowledgements

This work was financially supported by Project 911, Vietnam Ministry of Education and Training, and the University of Technology – Vietnam National University, Ho Chi Minh City.

References

1. C. Zhou and K. H. Low, “Design and locomotion control of a biomimetic underwater vehicle with Fin Propulsion,” *IEEE ASME Trans. Mechatron.* **17**(1), 25–35 (2012).
2. J. Yu and C. Zhang and L. Liu, “Design and control of a single-motor-actuated robotic fish capable of fast swimming and maneuverability,” *IEEE ASME Trans. Mechatron.* **21**(3), 1711–1719 (2016).
3. L. Hanlin and C. Oscar, “Swimming performance of a bio-inspired robotic vessel with undulating fin propulsion,” *Bioinspir. Biomim.* **13**(5), 056006 (2018).
4. R. Zhang, Z. Shen and Z. Wang, “Ostraciiform underwater robot with segmented caudal fin,” *IEEE Robot. Autom. Lett.* **3**(4), 2902–2909 (2018).
5. Z. Li, L. Ge, W. Xu and Y. Du, “Turning characteristics of biomimetic robotic fish driven by two degrees of freedom of pectoral fins and flexible body/caudal fin,” *Int. J. Adv. Robot. Syst.* **15**(1), 1729881417749950 (2018).
6. A. Krishnadas, S. Ravichandran and P. Rajagopal, “Analysis of biomimetic caudal fin shapes for optimal propulsive efficiency,” *Ocean Eng.* **153**, 132–142 (2018).
7. G. V. Lauder, E. J. Anderson, J. Tangorra and P. G. A. Madden, “Fish biorobotics: Kinematics and hydrodynamics of self-propulsion,” *J. Exp. Biol.* **210**(16), 2767–2780 (2007).
8. V. L. George, G. A. M. Peter, M. Rajat, D. Haibo and B. Meliha, “Locomotion with flexible propulsors: I. Experimental analysis of pectoral fin swimming in sunfish,” *Bioinspir. Biomim.* **1**(4), S25–S34 (2006).
9. L. Wang, M. Xu, B. Liu, K. H. Low, J. Yang and S. Zhang, “A three-dimensional kinematics analysis of a Koi Carp pectoral fin by digital image processing,” *J. Bion. Eng.* **10**(2), 210–221 (2013).
10. Z. Shiwu, L. Bo, W. Lei, Y. Qin, L. Kin Huat and Y. Jie, “Design and implementation of a lightweight bioinspired pectoral fin driven by SMA,” *IEEE ASME Trans. Mechatron.* **19**(6), 1773–1785 (2014).
11. Q. Yan, L. Wang, B. Liu, J. Yang and S. Zhang, “A novel implementation of a flexible robotic fin actuated by shape memory alloy,” *J. Bion. Eng.* **9**(2), 156–165 (2012).
12. C. K. Jeff, Jr., J. P. David and L. T. James, “Predicting propulsive forces using distributed sensors in a compliant, high DOF, robotic fin,” *Bioinspir. Biomim.* **10**(3), 036009 (2015).
13. J. L. Tangorra, C. J. Esposito and G. V. Lauder, “Biorobotic Fins for Investigations of Fish Locomotion,” *Proceedings of the IEEE/RSJ International Conference on Intelligent Robots and Systems*, St. Louis, MO, USA (2009) pp. 2120–2125.
14. W.-R. Hu, “Hydrodynamic study on a pectoral fin rowing model of a fish,” *J. Hydrodynam. B.* **21**(4), 463–472 (2009).
15. Y.-G. Xu and D.-C. Wan, “Numerical simulation of fish swimming with rigid pectoral fins,” *J. Hydrodynam. B.* **24**(2), 263–272 (2012).
16. S. B. Behbahani and X. Tan, “Role of pectoral fin flexibility in robotic fish performance,” *J. Nonlinear Sci.* **27**(4), 1155–1181 (2017).
17. S. B. Behbahani and X. Tan, “Bio-inspired flexible joints with passive feathering for robotic fish pectoral fins,” *Bioinspiration & Biomimetics* **11**(3), 036009 (2016).
18. S. B. Behbahani and X. Tan, “Design and modeling of flexible passive rowing joint for robotic fish pectoral fins,” *IEEE Trans. Robot.* **32**(5), 1119–1132 (2016).
19. B. Liu, Y. Yang, F. Qin and S. Zhang, “Performance study on a novel variable area robotic fin,” *Mechatronics.* **32**, 59–66 (2015).
20. J. Yu, M. Wang, H. Dong, Y. Zhang and Z. Wu, “Motion control and motion coordination of bionic robotic fish: A review,” *J. Bion. Eng.* **15**(4), 579–598 (2018).
21. R. W. Blake, “Influence of pectoral fin shape on thrust and drag in labriform locomotion,” *J. Zool.* **194**(1), 53–66 (1981).

22. K. Shoele and Q. Zhu, "Numerical simulation of a pectoral fin during labriform swimming," *J. Exp. Biol.* **213**(12), 2038–2047 (2010).
23. V. Kopman and M. Porfiri, "Design, modeling, and characterization of a miniature robotic fish for research and education in biomimetics and bioinspiration," *IEEE ASME Trans. Mechatron.* **18**(2), 471–483 (2013).
24. M. Aureli, V. Kopman and M. Porfiri, "Free-locomotion of underwater vehicles actuated by ionic polymer metal composites," *IEEE ASME Trans. Mechatron.* **15**(4), 603–614 (2010).
25. K. A. Morgansen, B. I. Triplett and D. J. Klein, "Geometric methods for modeling and control of free-swimming fin-actuated underwater vehicles," *IEEE Trans. Robot.* **23**(6), 1184–1199 (2007).
26. J. Wang, P. K. McKinley and X. Tan, "Dynamic modeling of robotic fish with a base-actuated flexible tail," *J. Dyn. Syst. Meas. Control.* **137**(1), 011004-011004-11 (2014).
27. J. Wang and X. Tan, "Averaging tail-actuated robotic fish dynamics through force and moment scaling," *IEEE Trans. Robot.* **31**(4), 906–917 (2015).
28. Y. Changlong, M. Shugen, L. Bin and W. Yuechao, "Turning and Side Motion of Snake-like Robot," *Proceedings of the IEEE International Conference on Robotics and Automation*, New Orleans, LA, USA (2004) pp. 5075–5080.
29. T. I. Fossen, *Guidance and Control of Ocean Vehicles*, (John Wiley & Sons Ltd., Chichester, England, 1994) pp. 40–42.
30. J. Wang and X. Tan, "A dynamic model for tail-actuated robotic fish with drag coefficient adaptation," *Mechatronics.* **23**(6), 659–668 (2013).
31. W. L. Chan and T. Kang, "Simultaneous determination of drag coefficient and added mass," *IEEE J. Oceanic Eng.* **36**(3), 422–430 (2011).
32. J. L. Kendall, K. S. Lucey, E. A. Jones, J. Wang and D. J. Ellerby, "Nature in engineering for monitoring the oceans: Comparison of the energetic costs of marine animals and AUVs," *Further Advances in Unmanned Marine Vehicles.* **77**, 373–405 (2012).
33. A. B. Phillips, M. Haroutunian, S. K. Man, A. J. Murphy, S. W. Boyd, J. I. R. Blake and G. Griffiths, "Mechanical and energetic factors underlying gait transitions in bluegill sunfish (Lepomis macrochirus)," *J. Exp. Biol.* **210**(24), 4265–4271 (2007).
34. A. P. Maertens, M. S. Triantafyllou and D. K. P. Yue, "Efficiency of fish propulsion," *Bioinspir. Biomim.* **10**(4), 046013 (2015).
35. R. W. Blake, "The mechanics of labriform locomotion II: An analysis of the recovery stroke and the overall fin-beat propulsive efficiency in the Angelfish," *J. Exp. Biol.* **85**, 337–342 (1980).
36. J. A. Walker, "Dynamics of pectoral fin rowing in a fish with an extreme rowing stroke: The threespine stickleback (Gasterosteus aculeatus)," *J. Exp. Biol.* **207**(11), 1925–1939 (2004).
37. P. E. Sitorus, Y. Y. Nazaruddin, E. Leksono and A. Budiyono, "Design and implementation of paired pectoral fins locomotion of labriform fish applied to a fish robot," *J. Bion. Eng.* **6**(1), 37–45 (2009).
38. M. Triantafyllou and G. Triantafyllou, "An efficient swimming machine," *Sci. Am.* **272**(3), 64–70 (1995).
39. J. M. Anderson, K. Streitlien, D. S. Barrett and M. S. Triantafyllou, "Oscillating foils of high propulsive efficiency," *J. Fluid Mech.* **360**, 41–72 (1998).
40. G. K. Taylor, R. L. Nudds and A. L. R. Thomas, "Flying and swimming animals cruise at a Strouhal number tuned for high power efficiency," *Nature.* **425**(6959), 707–711 (2003).
41. C. Eloy, "Optimal Strouhal number for swimming animals," *J. Fluids. Struct.* **30**, 205–218 (2012).
42. R. W. Blake, "The mechanics of labriform locomotion I. Labriform locomotion in the Angelfish (Pterophyllum Eimekei): An analysis of the power stroke," *J. Exp. Biol.* **82**(1), 255–271 (1979).

Appendix

$$\begin{aligned} \vec{n}_{K1} &= [-s(\psi+\theta_K)c(\gamma_{K1}) \;\; c(\psi+\theta_K)c(\gamma_{K1}) \;\; -s(\gamma_{K1})]^T, \\ \vec{n}_{K2} &= [s(\psi+\theta_K)c(\gamma_{K2}) \;\; -c(\psi+\theta_K)c(\gamma_{K2}) \;\; s(\gamma_{K2})]^T, \\ \vec{n}_{HK} &= [s(\psi+\theta_K) \;\; -c(\psi+\theta_K) \;\; 0]^T. \end{aligned} \tag{A1}$$

The linear velocity vector of the mass center of hinge base and fin panels:

$$\begin{aligned} v_{CHK} &= {}^W\dot{p}_{CHK}, \\ v_{CKk} &= {}^W\dot{p}_{CKk}. \end{aligned} \tag{A2}$$

The angular velocity vector of the mass center of hinge base and fin panels:

$$\begin{aligned} \omega_{CHK} &= {}^W\omega_B + {}^WR_B{}^B\omega_{HK}, \\ \omega_{Kk} &= ({}^W\omega_B + {}^WR_B{}^B\omega_{HK}) + {}^WR_{HK}{}^{HK}\omega_{Kk}, \end{aligned} \tag{A3}$$

where ${}^W\omega_B = [0, 0, \dot{\psi}]^T$; ${}^B\omega_{HK} = [0, 0, \dot{\theta}_K]^T$; ${}^{HL}\omega_{Lk} = [\dot{\gamma}_{Lk}, 0, 0]^T$; and ${}^{HR}\omega_{Rk} = [0, \dot{\gamma}_{Rk}, 0]^T$.

The involved rotational transformation matrixes are presented as follows:

$$\begin{aligned}
&{}^{W}R_{B}=\begin{bmatrix} c(\psi) & -s(\psi) & 0\\ s(\psi) & c(\psi) & 0\\ 0 & 0 & 1\end{bmatrix};\ {}^{B}R_{HL}=\begin{bmatrix} -c(\theta_L) & s(\theta_L) & 0\\ -s(\theta_L) & -c(\theta_L) & 0\\ 0 & 0 & 1\end{bmatrix};\\
&{}^{B}R_{HR}=\begin{bmatrix} -s(\theta_R) & -c(\theta_R) & 0\\ c(\theta_R) & -s(\theta_R) & 0\\ 0 & 0 & 1\end{bmatrix};\ {}^{HL}R_{L1}=\begin{bmatrix} 1 & 0 & 0\\ 0 & c(\gamma_{L1}) & -s(\gamma_{L1})\\ 0 & s(\gamma_{L1}) & c(\gamma_{L1})\end{bmatrix};\\
&{}^{HL}R_{L2}=\begin{bmatrix} 1 & 0 & 0\\ 0 & s(\gamma_{L2}) & c(\gamma_{L2})\\ 0 & -c(\gamma_{L2}) & s(\gamma_{L2})\end{bmatrix};\ {}^{HR}R_{R1}=\begin{bmatrix} c(\gamma_{R1}) & 0 & s(\gamma_{R1})\\ 0 & 1 & 0\\ -s(\gamma_{R1}) & 0 & c(\gamma_{R1})\end{bmatrix};\\
&{}^{HR}R_{R2}=\begin{bmatrix} -s(\gamma_{R2}) & 0 & c(\gamma_{R2})\\ 0 & 1 & 0\\ -c(\gamma_{R2}) & 0 & -s(\gamma_{R2})\end{bmatrix}.
\end{aligned}\tag{A4}$$

Coordinate vector of a point on the neutral axis of fin and hinge bases ${}^{W}p_{Kk}$, ${}^{W}p_{HK}$:

$$\begin{bmatrix} {}^{W}p_{Kk}\\ 1\end{bmatrix}={}^{W}P_{Kk};\ \begin{bmatrix} {}^{W}p_{HK}\\ 1\end{bmatrix}={}^{W}P_{HK}\tag{A5}$$

with

$$\begin{aligned}
&{}^{W}P_{R1}={}^{W}g_{R1}\begin{bmatrix} 0\\ (L_0+\ell)\\ \frac{d_s}{2}+\ell\frac{d_p-d_s}{2L}\\ 1\end{bmatrix};\ {}^{W}P_{R2}={}^{W}g_{R2}\begin{bmatrix} \frac{d_s}{2}+\ell\frac{d_p-d_s}{2L}\\ (L_0+\ell)\\ 0\\ 1\end{bmatrix};\\
&{}^{W}P_{L1}={}^{W}g_{L1}\begin{bmatrix} (L_0+\ell)\\ 0\\ \frac{d_s}{2}+\ell\frac{d_p-d_s}{2L}\\ 1\end{bmatrix};\ {}^{W}P_{L2}={}^{W}g_{L2}\begin{bmatrix} (L_0+\ell)\\ \frac{d_s}{2}+\ell\frac{d_p-d_s}{2L}\\ 0\\ 1\end{bmatrix};
\end{aligned}$$

$${}^{W}g_{Kk}={}^{W}g_{B}.{}^{B}g_{HK}.{}^{HK}g_{Kk},\tag{A6}$$

where

$${}^{W}g_{B}=\begin{bmatrix} {}^{W}g_{B} & {}^{W}d_{B}\\ O & 1\end{bmatrix};\ {}^{W}d_{B}=\begin{bmatrix} X\\ Y\\ 0\end{bmatrix};$$

$${}^{B}g_{HK}=\begin{bmatrix} {}^{B}g_{HK} & {}^{B}d_{HK}\\ O & 1\end{bmatrix};\ {}^{B}d_{HL}=\begin{bmatrix} a_1\\ b_1\\ 0\end{bmatrix};\ {}^{B}d_{HR}=\begin{bmatrix} a_1\\ -b_1\\ 0\end{bmatrix};\ {}^{B}d_{HR}=\begin{bmatrix} a_1\\ -b_1\\ 0\end{bmatrix};$$

$${}^{HK}g_{Kk}=\begin{bmatrix} {}^{HK}g_{Kk} & {}^{HK}d_{Kk}\\ O & 1\end{bmatrix};\ {}^{HK}d_{K1}=\begin{bmatrix} 0\\ 0\\ \frac{b_H}{2}\end{bmatrix};\ {}^{HK}d_{K2}=\begin{bmatrix} 0\\ 0\\ -\frac{b_H}{2}\end{bmatrix}.$$

Coordinate vectors ${}^{W}p_{CKk}$ and ${}^{W}p_{CHK}$ corresponding to the mass centroid of fin panels and hinge base can be obtained by substituting $\ell=c_L$ into Eq.(A5)

$$\begin{bmatrix} {}^{W}p_{CKk}\\ 1\end{bmatrix}={}^{W}P_{CKk};\ \begin{bmatrix} {}^{W}p_{CHK}\\ 1\end{bmatrix}={}^{W}P_{CHK}.\tag{A7}$$

The inertia moment of hinges and fin panels:

$$I_{HR}=\begin{bmatrix} I^w_{CH} & 0 & 0 \\ 0 & I^l_{CH} & 0 \\ 0 & 0 & I^t_{CH} \end{bmatrix};\ I_{R1}=\begin{bmatrix} I^t_{CF} & 0 & 0 \\ 0 & I^l_{CF} & I^e_{CF} \\ 0 & I^e_{CF} & I^w_{CF} \end{bmatrix};\ I_{R2}=\begin{bmatrix} I^w_{CF} & I^e_{CF} & 0 \\ I^e_{CF} & I^l_{CF} & 0 \\ 0 & 0 & I^t_{CF} \end{bmatrix};$$
$$I_{HL}=\begin{bmatrix} I^l_{CH} & 0 & 0 \\ 0 & I^w_{CH} & 0 \\ 0 & 0 & I^t_{CH} \end{bmatrix};\ I_{L1}=\begin{bmatrix} I^l_{CF} & 0 & I^e_{CF} \\ 0 & I^t_{CF} & 0 \\ I^e_{CF} & 0 & I^w_{CF} \end{bmatrix};\ I_{L2}=\begin{bmatrix} I^l_{CF} & I^e_{CF} & 0 \\ I^e_{CF} & I^w_{CF} & 0 \\ 0 & 0 & I^t_{CF} \end{bmatrix}. \tag{A8}$$

The useful power and input power elements are, respectively, calculated as follows:

$$\bar{P}_o=\frac{1}{T_w}\int_{t_0}^{t_0+T_w} F_{Tx}(t)v_x(t)dt, \tag{A9}$$

$$\bar{P}_i=\frac{1}{T_w}\int_{t_0}^{t_0+T_w}\left(\tau_R(t)\dot{\theta}_R(t)+\tau_L(t)\dot{\theta}_L(t)\right)dt, \tag{A10}$$

$$\bar{P}_{mi}=\frac{1}{T_w}\int_{t_0}^{t_0+T_w}\left(-\int_0^{L_0+L}(v_{HL}dF_{HL}+v_{HR}dF_{HR})-\sum_{k=1}^{2}\int_0^{L}(v_{Lk}dF_{Lk}+v_{Rk}dF_{Rk})\right), \tag{A11}$$

where F_{Tx} denotes the total thrust along x_B-axis produced by the pectoral fins: $F_{Tx}=T_Rs(\theta_R)+T_Ls(\theta_L)$.